

Case History

Analysis of time-lapse data error in complex conductivity imaging to alleviate anthropogenic noise for site characterization

Adrian Flores Orozco¹, Andreas Kemna², Andrew Binley³, and Giorgio Cassiani⁴

ABSTRACT

Previous studies have demonstrated the potential benefits of the complex conductivity (CC) imaging over electrical resistivity tomography for an improved delineation of hydrocarbon-impacted sites and accompanying biogeochemical processes. However, time-lapse CC field applications are still rare, in particular for measurements performed near anthropogenic structures such as buried pipes or tanks, which are typically present at contaminated sites. To fill this gap, we have developed CC imaging (CCI) results for monitoring data collected in Trecate (northwest Italy), a site impacted by a crude oil spill. Initial imaging results reveal only a poor correlation with seasonal variations of the groundwater table at the site (approximately 6 m). However, it is not clear to which extent such results are affected by anthropogenic structures present at the site. To address this, we performed a detailed analysis of the

misfit between direct and reciprocal time-lapse differences. Based on this analysis, we were able to discriminate spatial and temporal sources of systematic errors, with the latter commonly affecting measurements collected near anthropogenic structures. Following our approach, CC images reveal that temporal changes in the electrical properties correlate well with seasonal fluctuations in the groundwater level for areas free of contaminants, whereas contaminated areas exhibit a constant response over time characterized by a relatively high electrical conductivity and a negligible polarization effect. In accordance with a recent mechanistic model, such a response can be explained by the presence of immiscible fluids (oil and air) forming a continuous film through the micro and macropores, hindering the development of ion-selective membranes and membrane polarization. Our results demonstrate the applicability of CCI for an improved characterization of hydrocarbon-contaminated areas, even in areas affected by cultural noise.

INTRODUCTION

Management of hydrocarbon-impacted sites, in particular the design of adequate remediation strategies, encourages the development of new methodologies for the spatial characterization of contaminant plumes and associated biogeochemical processes (e.g., Schädler et al., 2012). Ideally, the characterization techniques should help to define the geometry of the hydrogeologic units and the extent of the contaminant plumes with enhanced resolution,

as well as assess possible biogeochemical transformations of contaminants. To date, site characterization relies mainly on laboratory analysis of gas, soil, and groundwater samples. Although *ex-situ* analysis provides the direct measurement of the parameters of interest (e.g., chemical concentrations), investigations using direct methods are strongly limited by the sampling procedure (i.e., location and volume), thus, reducing the resolution of the investigation — given the spatial and temporal variability of the observed phenomena (e.g., Atekwana and Atekwana, 2010). In most cases,

Manuscript received by the Editor 15 November 2017; revised manuscript received 27 September 2018; published ahead of production 13 December 2018; published online 05 March 2019.

¹TU-Wien, Department of Geodesy and Geoinformation, Geophysics Research Division, Vienna, Austria. E-mail: flores@tuwien.ac.at (corresponding author).

²University of Bonn, Steinmann Institute, Department of Geophysics, Bonn, Germany. E-mail: kemna@geo.uni-bonn.de.

³Lancaster University, Lancaster Environment Centre, Lancaster, UK. E-mail: a.binley@lancaster.ac.uk.

⁴University of Padova, Department of Geosciences, Padova, Italy. E-mail: giorgio.cassiani@unipd.it.

© 2019 Society of Exploration Geophysicists. All rights reserved.

ex-situ investigations rely on the interpretation of too few and largely spaced sampling points requiring the interpolation of the data, which may then not reflect the actual geometry of, e.g., the contaminant plumes, making the relevant interpretations weak and potentially misleading. Furthermore, the collection of samples and laboratory analyses are time-consuming, causing the site characterization to last several months (or even years), potentially resulting in the comparison of data collected under different hydro-geochemical conditions.

Several studies have investigated the applicability of geophysical methods for site characterization taking into account the possibility to gain quasicontinuous spatiotemporal information about the subsurface properties. In particular, given the significant contrasts in the electrical properties between hydrocarbon contaminants (typically associated with low electrical conductivity) and groundwater (low to intermediate electrical conductivity), several studies have suggested the application of electrical resistivity tomography (ERT) (e.g., Sauck, 2000; Chambers et al., 2005; Heenan et al., 2014; Naudet et al., 2014). Nevertheless, over the past two decades, extensive laboratory and field studies have demonstrated that the electrical response of mature hydrocarbon plumes might reveal high electrical conductivity values following biotic and abiotic transformations of the contaminants (for details, we refer to the revision from Atekwana and Atekwana, 2010). Hydrocarbons can act as an energy source promoting microbial growth and the release of metabolic products, such as carbonic acids. Hence, the anomalous high electrical conductivity values observed in mature hydrocarbon plumes have mainly been attributed to an increase in the ionic concentration, and, thus, the fluid electrical conductivity σ_w accompanying the accumulation of carbonic acids (e.g., Cassidy et al., 2001; Werkema et al., 2003; Atekwana et al., 2004). Moreover, carbonic acids may contribute to the weathering of grain surfaces and enhancement of secondary porosity, further increasing the σ' observed in ERT surveys (e.g., Abdel Aal et al., 2006; Atekwana and Atekwana, 2010).

In addition to this, field investigations have also demonstrated the applicability of the complex electrical conductivity (CC), an extension of the ERT method, for improved site characterization (e.g., Kemna et al., 2004; Schmutz et al., 2010; Revil et al., 2011; Deceuster and Kaufmann, 2012; Johansson et al., 2015), and the characterization of the source zone and plume of contaminants (e.g., Flores Orozco et al., 2012a). The CC imaging (CCI) results are expressed in terms of its real σ' and imaginary σ'' components, which refers to the electrical conductivity and capacitive properties of the subsurface, respectively (e.g., Marshall and Madden, 1959; Slater and Lesmes, 2002; Kemna et al., 2012). For geologic media free of metallic minerals, the conductivity is mainly controlled by the saturation σ_w , the connectivity of the pore space (e.g., Archie, 1942), and by surface-conduction processes taking place at the grain-water interface (e.g., Slater and Lesmes, 2002; Slater et al., 2007; Kemna et al., 2012). The imaginary component σ'' is only caused by the polarization of charges in the electrical double layer (EDL) built at the interface between grain and pore water (e.g., Marshall and Madden, 1959; Kemna et al., 2012).

Initial studies (e.g., Olhoeft, 1985; Vanhala, 1997; Kemna et al., 2004) revealed a significant increase in the polarization effect with increasing concentrations of aromatic hydrocarbons (e.g., toluene, kerosene). These are “nonpolar” compounds, which are unable to interact with water molecules, due to their lack of ionic or polar groups. Hence, in the subsurface, they form immiscible droplets

caged within the water filling pores, without direct contact with the grain surface, and thus, are referred to as nonwetting oil. Accordingly, Schmutz et al. (2010) propose a modification of the model describing the polarization of the EDL, formed at the grain-fluid interface, to include the effect of the nonwetting hydrocarbons. Such a model predicts an increase in the polarization response with increasing the volumetric content of nonwetting hydrocarbons.

Contrary to previous studies, Ustra et al. (2012) report a negligible polarization response in laboratory measurement with sand-clay mixtures for different toluene concentrations. At the field scale, Flores Orozco et al. (2012a) observed an initial increase in the polarization response with increasing the concentrations of benzene and toluene, consistent with the response observed in the laboratory by Schmutz et al. (2010). However, the polarization response fades for contaminant concentrations above the saturation concentration (i.e., the occurrence of hydrocarbons as the free-phase), in agreement with the response observed by Ustra et al. (2012). Johansson et al. (2015) also observed similar results in field measurements in a site impacted by perchloroethylene, an “oil-wetting” hydrocarbon. Moreover, Cassiani et al. (2009) observe an inconclusive response for laboratory measurements performed in sand samples mixed with different concentrations of crude oil.

An extension to previous experiments, Revil et al. (2011) reported the decrease in the polarization response with increasing the volumetric content of polar compounds, or oil-wetting hydrocarbons, i.e., the scenario when the oil is in direct contact with the grain surface. However, such observations does not explain the observed increase in the polarization response at low hydrocarbon concentrations observed in field studies (e.g., Flores Orozco et al., 2015). An increase in the polarization response for aged hydrocarbon plumes, in laboratory studies, has been related to the accumulation of negatively charged microbial cells (e.g., Abdel Aal et al., 2006; Atekwana and Slater, 2009; Revil et al., 2012). However, biostimulation experiments at the field scale reported negligible changes in the polarization effects following biofilm formation, but a much larger response due to the precipitation of minerals accompanying microbial activity (e.g., Flores Orozco et al., 2011, 2013). Therefore, recently it has been suggested that the increase in the polarization effect observed in aged hydrocarbon contaminant plumes might be related to the precipitation of metallic minerals accompanying microbial activity (Mewafy et al., 2013; Abdel Aal et al., 2014). Moreover, changes in the chemical composition of groundwater, as well as the accumulation of metabolic by-products (e.g., organic acids), can also modify the surface properties in the hydrocarbons (e.g., Cassidy et al., 2001), for instance, promote the changes from nonwetting oil to oil-wetting, thus resulting in modifications of the geophysical response.

The noteworthy differences observed in laboratory and field investigations clearly demonstrate the necessity for further investigations to better evaluate the applicability of the CCI method and improve the interpretation of the imaging results. Monitoring studies at the field scale are necessary to understand the dynamics in the geophysical response, considering the impossibility to reproduce in the laboratory the variety of processes taking place (simultaneously) in hydrocarbon-impacted sites. Moreover, existing field studies have been conducted in areas without anthropogenic structures. However, hydrocarbon contaminants are typically located at (often derelict) industrial areas and they are commonly associated with their proximity to anthropogenic structures, such as power lines,

or buried pipes and tanks. The electrical response of such anthropogenic structures may mask the one of the subsurface, thus hindering an adequate interpretation of the CCI results and its application for site characterization. Therefore, field investigations need to address the capabilities of the CCI method to discriminate between signatures due to anthropogenic structures, lithology, and contaminants, as required for an improved site characterization.

In this study, we present the results of one-year CC monitoring measurements collected at a site impacted by a crude oil spill. Petroleum crude oil is a light nonaqueous phase liquid (LNAPL) mainly composed of nonpolar compounds; thus, it is expected to result in an increase in the polarization response with increasing the concentration (at least at early stages), after the model by [Schmutz et al. \(2010\)](#). Strong variations in the depth to the groundwater table at the site permitted the investigation of changes in the electrical response due to the vertical transport of the contaminant and biogeochemical processes. Extensive geochemical data have been collected since the time of an oil spill accident in 1994. Such data are necessary to constrain the interpretation of CCI results. At the site, relatively few anthropogenic structures are present; yet, their response can distort or mask the electrical signatures associated with the lithology and contaminant. Considering that such distortions might also control temporal fluctuations in the measured data, anthropogenic structures can then be defined as sources of temporal error. To better investigate this, we performed a detailed analysis of the time-lapse data-error, aiming at the identification and removal of spatial and temporal outliers (i.e., systematic errors) and the quantification of uncertainties in CC monitoring measurements. The analysis of the data presented here aims at evaluating the possibility of minimizing the distortion due to cultural noise in CC monitoring images in areas impacted by high hydrocarbon concentrations, a step forward for soil contamination assessment and site characterization.

MATERIAL AND METHODS

Study area

The study area is located close to Trecate (Novara, Italy), where a blowout from a deep oil well in February 1994 resulted in the spill of approximately 15,000 m³ of crude oil ([Cassiani et al., 2014](#)). The subsequent site remediation has been reported, for example, in the study of [Brandt et al. \(2002\)](#). The area is mainly agricultural with a prevalence of man-made rice paddies, partly converted to other crops, such as soy and maize. The main zone of hydrocarbon contamination covers approximately 96 ha, affecting the soil, vadose zone, and groundwater. The saturated and unsaturated zones have been monitored for natural attenuation and evolution of contamination conditions since the time of the accident. Measurable levels of hydrocarbon contamination have been observed in soil samples collected at different depths between 2 and 10 m below ground surface (bgs) between 1995 and 2007. Figure 1 shows the

total petroleum hydrocarbon (TPH) volumetric content in the soil as reported from chemical analysis of samples collected at more than 115 points, distributed at depths of 2, 6, and 10 m bgs and sampled using direct-push techniques. The groundwater samples collected in the contaminated area show a brown oil phase emulsion in the aqueous phase, and high dissolved hydrocarbon concentrations limited essentially to the same area of elevated contamination in the soil at 10 m in depth, shown in Figure 1. Further spread of the contaminant plume in groundwater downstream (approximately southeast) of the site is strongly limited by strong biodegradation of the hydrocarbons, as shown, e.g., by the study of [Burberry et al. \(2004\)](#). The contamination in the soil is likely to have been controlled over the years by the strong seasonal water table oscillations between 6 and 12 m bgs, which produces a clear smear zone, also spreading the contaminant laterally at greater depths (see Figure 1).

Geologically, the site is characterized by a thick sequence of poorly sorted silty sands and gravels in extensive lenses, typical of braided river sediments ([Cassiani et al., 2004](#)). Braided rivers are related to high energy but are also typical of environments that dramatically decrease the channel depth and velocity, and, thus could lead to the intercalation of fine sediments, such as clay ([Williams and Rust, 1969](#)). Such intercalations lead to the formation of paleochannels at the site, which can be found now filled by fine

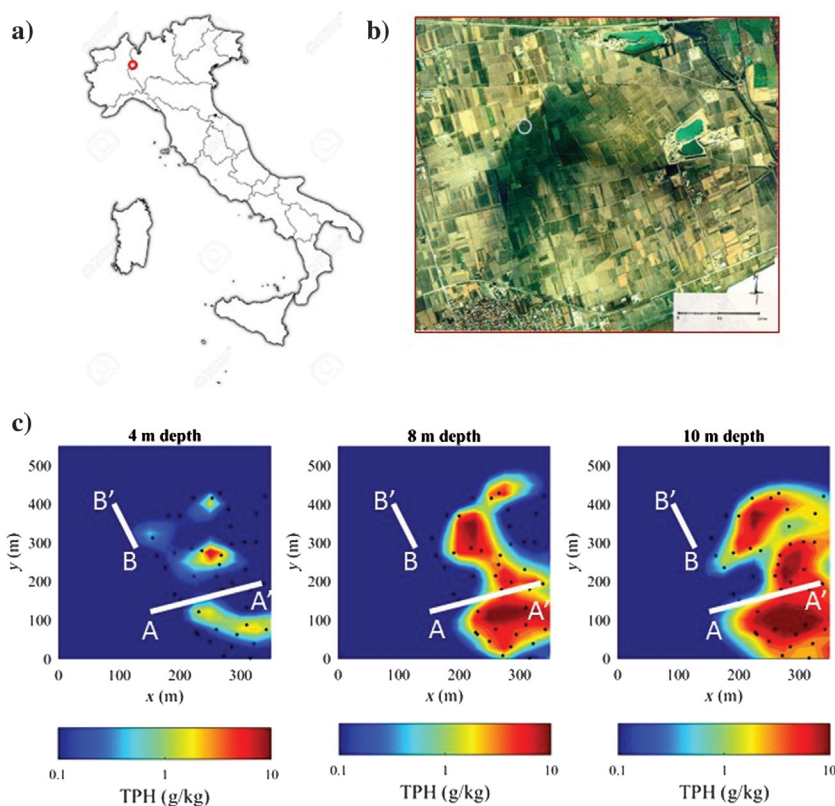


Figure 1. (a) The location of the study area, (b) satellite image revealing the extension of the contaminant plume at the surface following the crude oil well blowout in 1994, and (c) contaminant distribution in the subsurface at different depths as obtained from the chemical analysis of soil samples (black dots). The contaminant concentrations are expressed in terms of the TPH per unit soil mass. CC monitoring data sets were collected in lines A-A' (west-east) and B-B' (south-north) indicated by the solid white lines. Note that line B-B' lies in the uncontaminated area; thus, it can be considered as a "blank" line, whereas line A-A' crosses a heavily contaminated zone.

sediments (clay and silt), as discussed by Cassiani et al. (2004). Additionally, an artificial layer of clayey-silty material, approximately 1–2 m thick, placed as a liner for rice paddies about a century ago, overlies most of the site (Cassiani et al., 2014). The seasonal fluctuation in the water table is primarily a result of recharge from regional irrigation and flooding of the rice paddies. During the experiments presented here, the depth to the water table was observed at its maximum by the end of February (10.5 m bgs) and at its minimum at the end of September (5 m bgs). Further details on the site can be found in the study by Cassiani et al. (2014).

Complex conductivity monitoring measurements

The CC method — also known as the induced polarization (IP) method — is based on measurements using a four-electrode array, where two electrodes are used to inject electric current and the other two are used to measure the resulting electrical voltages. In the present study, measurements were collected in the time domain with a Syscal Pro (IRIS Instruments, France) using a square wave with a 50% duty cycle and a pulse length of 2 s. Integral chargeability readings were performed between 240 and 1840 ms after shutting current injection off using a linear distribution of 20 windows. Measurements were conducted using stainless steel electrodes with a separation of 2.5 m and a dipole-dipole “skip-3” configuration for a dipole length of 10 m (i.e., the dipole length defined by the number of skipped electrodes along the electrode array) to reach an estimated depth of investigation of approximately 12 m.

Monitoring measurements were collected along the two lines shown in Figure 1: (1) Line A-A', using a total of 81 electrodes in a roll-along scheme (an extension of 33 electrodes) for a total length of 200 m, with a rough west–east orientation, the latter designed to cover areas from negligible to high contaminant concentrations; and (2) line B-B', a control line deploying a total of 48 electrodes for a length of 117.5 m, approximately oriented south–north and located in the uncontaminated area of the site (Figure 1). Measurements were collected every two months, starting in May 2009 and with the last data set collected in February 2010. All data sets were collected as direct-reciprocal pairs for data error (ϵ) analysis, with reciprocal readings referred to the recollection of the data after interchanging current and potential dipoles. Error analysis of independent data sets (i.e., collected at each time) was performed following the methodology described by Flores Orozco et al. (2012b). Additionally, we present here a methodology aiming at characterizing the data error in time-lapse differences.

Inversion of the data was performed using CRTomo, a smoothness-constrained inversion algorithm by Kemna (2000). The code solves for the distribution of the complex electrical resistivity ρ^* , the inverse of the CC ($\sigma^* = 1/\rho^*$) from a tomographic electrical impedance data sets Z^* . Hence, integral chargeability measurements were linearly converted to electrical impedance phase-shift values using the approach of Kemna et al. (1997) assuming a constant phase response (at the fundamental frequency of 0.125 Hz). The assumption of a constant-phase response is valid considering the relatively narrow frequency-range for the measurements of the integral chargeability, equivalent to approximately 0.5–4 Hz. To account for the known geologic layering at the site (Cassiani et al., 2004, 2014), all inversions presented here were performed using a preferential horizontal smoothing with a ratio of 40:1 of the horizontal versus the vertical smoothing parameters (for details in the implementation, see, e.g., Kemna et al., 2002).

To avoid the interpretation of model parameters with a poor sensitivity, we blanked in the imaging results those pixels associated with cumulated sensitivity values two orders of magnitude smaller than the highest cumulated sensitivity (i.e., the sum of absolute, data-error weighted, sensitivities of all considered measurements; see, e.g., Kemna et al., 2002; Weigand et al., 2017).

Complementary geophysical data

To assess lateral variations of the electrical properties at the site, mapping measurements were conducted with low-induction-number electromagnetic (EMI) methods using a CMD-4 (GF Instruments, Czech Republic), which has an effective depth of investigation of 6 m.

To support the interpretation of the CCI results, ground-penetrating radar (GPR) data sets were collected along the same CC monitoring profiles using a PulseEKKO Pro system (Sensors & Software, Canada) with 100 MHz antennas. The GPR surface profiles presented here were based on a common-offset acquisition. Borehole GPR data, also using 100 MHz antennas, were collected with two schemes: (1) a multiple offset gather with 0.5 m vertical spacing between antenna stations and (2) a zero-offset profile (ZOP) with 0.25 m spacing between antenna stations. The complete description of the GPR processing and results is presented in the study of Cassiani et al. (2014).

To better differentiate in this study between the different geophysical data and modeled quantities, CCI results are presented in terms of its real σ' and imaginary σ'' components, whereas the measurements are represented by the apparent resistivity ρ_a and phase-shift φ_a . The EMI mapping data are presented in terms of the measured apparent conductivity σ_a because we are only interested in the lateral changes.

RESULTS AND DISCUSSIONS

Baseline characterization

Figure 2 presents the imaging results in terms of the electrical conductivity (expressed in terms of the real component of the CC, σ') and polarization (expressed in terms of the imaginary component of the CC, σ''), as solved for baseline measurements collected in May 2009, related to a groundwater level located at 6 m bgs. The electrical images for the control line (B-B') exhibit the lowest values in the electrical conductivity (σ' : approximately 1 mS/m), and a modest polarization effect (σ'' : approximately 10–20 μ S/m). A similar response is also observed in the first 60 m along the A-A' profile, which corresponds to the clean area. Variations in the CC at depth in line B-B' appear to be controlled by lithologic changes, for instance, the areas associated with the lowest polarization effect (σ'' : approximately 20 μ S/m) and conductivity values (σ' : < 1 mS/m) reveal poor agreement with the location of the groundwater level, yet they are consistent with intercalations of unsaturated silty sands and saturated gravels (e.g., between 5 and 10 m in depth). To aid in the interpretation of the electrical signatures, we present in Figure 2 the lithologic description from a core recovered during the drilling of a well in the vicinity of line B-B' (borehole BB reported in Cassiani et al., 2004). Moreover, CC images for line B-B' illustrate lateral variations in the thickness of the geologic units, associated with the existence of paleochannels at the site typical of braided river environments. Lateral variations in

the electrical properties resolved for profile B-B' are consistent with previous observations at the site (Cassiani et al., 2004).

Electrical values associated with the contaminated area of profile A-A' (between 60 and 200 m along the profile direction) reveal different anomalies in σ' and σ'' . The most prominent structures are marked in Figure 2 and can be summarized as (1) two shallow anomalies characterized by modest conductive and high polarization values, located approximately 60 and 100 m along the profile direction; (2) an anomaly between 1 and 5 m depth and between approximately 60 and 100 m along the profile direction revealing the lowest conductivity values and lateral changes from high to low polarization values; and (3) a shallow anomaly in the unsaturated zone exhibiting the highest σ' and σ'' values between 120 and 180 m along the profile direction. The last anomaly also reveals a vertical transition to a deeper structure characterized by low polarization effect ($\sigma'' < 5 \mu\text{S/m}$) in the saturated zone.

To help with the interpretation of the anomalies observed in the CC images, we present in Figure 3 the map of the apparent electrical conductivity σ_a as obtained from the EMI measurements, as well as the common-offset GPR

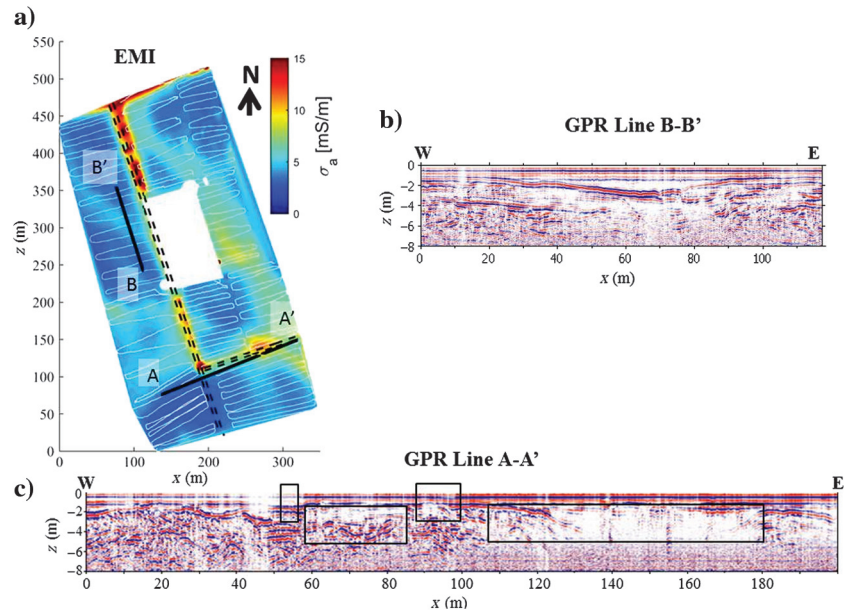


Figure 3. Complementary geophysical data sets: (a) Interpolated map of the apparent electrical conductivity σ_a measured with EMI at a nominal depth of investigation of 6 m with the position of the EMI readings indicated by the white dots, the location of the profile A-A' and B-B' by the solid black lines, and unpaved roads by the dashed lines; common offset GPR profile along line (b) B-B' and (c) A-A'. The anomalies depicted by the solid lines in the GPR profile for line A-A' indicates the position of the anomalies observed in the CCI results.

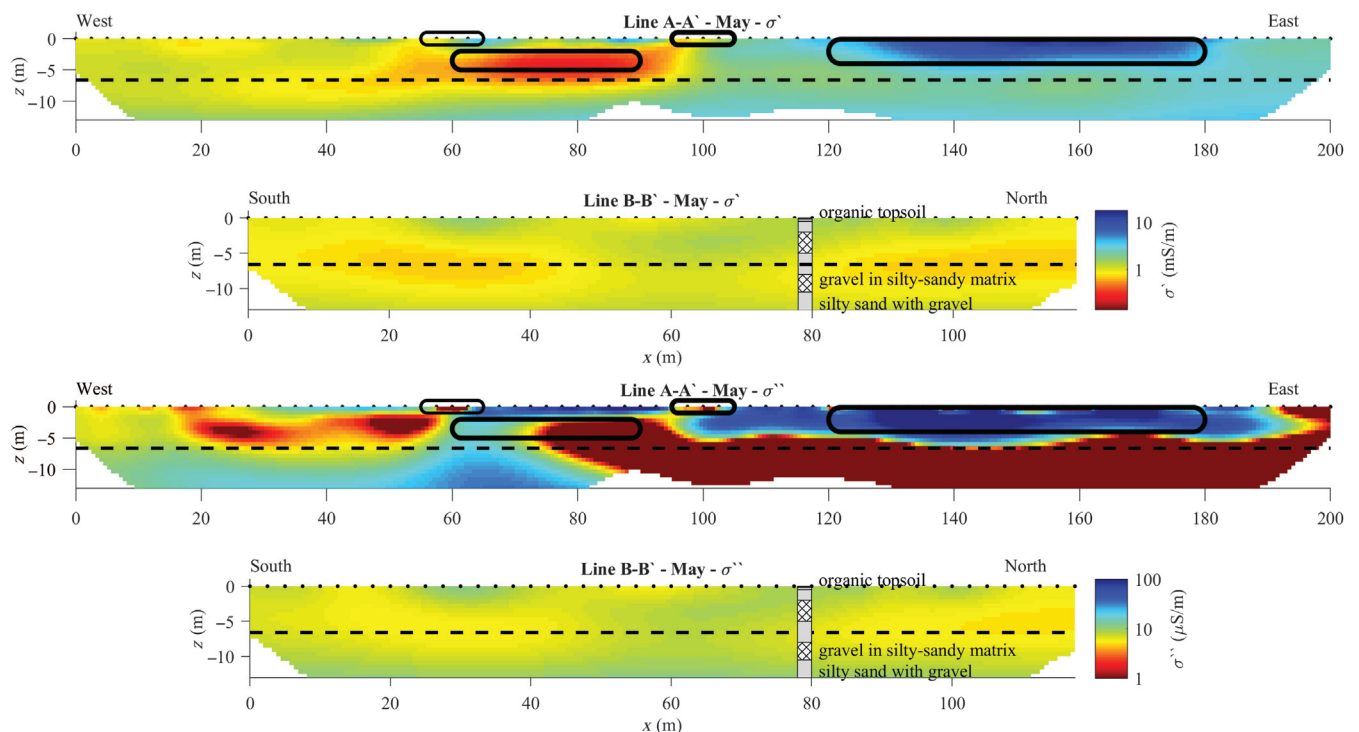


Figure 2. The CCI results for baseline measurements (May 2009) collected along lines A-A' and B-B', expressed in terms of the real σ' and imaginary σ'' components of the CC. The water table at the time of acquisition is shown by the dashed black line, and the position of the electrodes is marked with the solid dots at the surface. Anomalies marked by the solid lines along profile A-A' refer to possible anthropogenic structures, whereas available lithologic information from previous drillings is imposed at the corresponding position in profile B-B'.

profiles for measurements along lines A-A' and B-B'. The position of the CC anomalies is also marked in the radargram presented in Figure 3. The apparent conductivity σ_a map presented in Figure 3a clearly reveals high σ_a anomalies in the vicinity of profile A-A'. In particular, the elongated feature roughly oriented north–south between 150 and 300 m in the x -direction of the EMI map. Such an anomaly is coincident with the position of an unpaved road. Due to the compacted materials at the surface, such roads are expected to result in low electrical conductivity values. The high σ_a anomaly observed in Figure 3a might indicate the location of at least one buried pipe. The unpaved road crosses line A-A' at approximately 60 m, where the GPR image (Figure 3c) reveals shallow reflections, as expected for measurements near metallic structures, confirming the position of a possible pipe. Moreover, similar reflections are observed in the near surface at approximately 95 m, pointing out the presence of a second anthropogenic structure. This is the location of the shallow anomaly (a) observed in the CC images (see Figure 2), characterized by modest σ' , and high σ'' values. City documents indicate the location of a cast iron water pipe. Yet, no information is available about its exact size, nor about the possible coating, which is a common method used to prevent oxidation.

In addition to the interpreted pipe, the CC images reveal an anomaly characterized by a high polarization response between 60 and 80 m (along line A-A') also consistent with reflection hyperbolas observed in the GPR profile (between approximately 2 and 5 m bgs), as well as with high σ_a values in EMI measurements. Although such an anomaly may be interpreted as possible further anthropogenic structures, the deep extension of the anomaly might also be indicative of a lithologic contact. At present, no information is available to aid in the interpretation.

Furthermore, the lack of reflections in the radargram of line A-A', between 120 and 180 m, spatially corresponds to the high σ_a , σ' , and σ'' values in the EMI and CC images and thus can be explained by the attenuation of EMI waves in conductive media (von Hippel, 1954). Such an observation suggests the presence of a clay-rich layer that is likely to be the filling of a paleochannel of a braided river. Traces of these channels can be also seen in Figure 3a as relatively more conductive features elongated roughly in the north-northwest–south-southeast direction, with the bottom of one such channel clearly visible in the GPR line along B-B' (for a more detailed discussion, see Cassiani et al., 2004). Alternatively, this anomaly may be interpreted as the result of an increase in fluid conductivity accompanying the accumulation of carbonic acids accompanying the well-documented degradation of hydrocarbons at the site (e.g., Burberry et al., 2004). Accordingly, the increase in σ'' could be explained by the expected increase in the polarization response with increasing contaminant concentration predicted by the model from Schmutz et al. (2010).

In contrast to line A-A', the control line B-B' does not reveal indications of possible anthropogenic structures and exhibits only vertical interfaces between 4 and 8 m bgs reflecting the sand and gravel intercalations, which are consistent in both GPR and CC images, as well as with the lateral variations observed in the EMI between low and moderate σ_a values.

Cultural noise in CC monitoring results

An initial analysis of the inversion results, based on the independent analysis of monitoring data sets collected along line A-A' revealed inconclusive spatial and temporal patterns, hindering their

interpretation (Appendix A). Whereas the σ' monitoring images show relatively minimal variations for data collected at different periods, the polarization images show significant temporal variations, especially in the uncontaminated area. This region shows, in general, high σ'' values in the saturated zone, with vertical variations along the monitoring period well-correlated with changes in the groundwater table. Although promising, imaging results in the uncontaminated area resolved for November do not reflect the shallow position of the groundwater. Moreover, in the contaminated area of profile A-A' (between 60 and 200 m), the response is practically constant along the entire monitoring experiments. The apparent lack of variations in the electrical monitoring images for the contaminated areas may be indicative of (1) a constant response over time due to the contaminant plume, (2) electrical signatures being controlled by static (i.e., time-invariable) subsurface properties such as the lithology, or (3) the presence of anthropogenic structures (such as the water pipe) masking the electrical response of subsurface materials and contaminants.

Accounting for the time-lapse differences between the monitoring and the baseline images should permit to mute the effect due to lithology and anthropogenic structures, assuming that those do not change over the monitoring time (e.g., Kemna et al., 2002). A further alternative may be given by the direct inversion of the time-lapse differences, or the inversion of the data using temporal regularization (e.g., Lesparre et al., 2017). However, the presence of systematic errors in the data, as well as cultural noise, might mislead the application of such approaches. Hence, the quantification of random errors is critical for an adequate performance of time-lapse differences and time-regularization inversion schemes (Lesparre et al., 2017). In the case of the Trecate monitoring data sets, anthropogenic structures such as the unpaved road and the water pipe represent important sources of error. Moreover, monitoring measurements can also be affected by further sources of systematic errors related to the comparison of data collected with varying contact resistance of the electrodes, which can arise due to variations in temperature, surface moisture, or the presence of snow and ice in the surface during the winter measurements.

To overcome these deficiencies and improve the resolution of the electrical images, it is critical to (1) identify and remove outliers (i.e., systematic errors) and (2) quantify random error in the measurements, which can be taken into account within the inversion (e.g., Kemna, 2000; Flores Orozco et al., 2012b; Binley et al., 2016). In particular, for this study, we consider outliers to be not only related to spatially inconsistent in the independent measurements, but also, and most importantly, to data errors in the time-lapse differences for the CC measurements collected over the monitoring period, which hereafter are referred to as temporal outliers. Such temporal outliers are related to misplaced electrodes, variations in surface properties, and the contact resistance as well as to possible changes in the signatures of anthropogenic structures.

Raw-data analysis and identification of spatial and temporal outliers

Analysis of each independent data set (i.e., tomographic data collected at each time during the monitoring period) shows a good reciprocity for measurements along profile A-A', as presented in Figure 4 in terms of the apparent resistivity ρ_a and the apparent phase-shift ϕ_a . The plots in Figure 4 show the highest ($|\phi_a| > 20$ mrad) values between electrodes 32 and 48, which

include variations from large negative to large positive values. The collection of anomalous positive phase-shift values in electrical impedance measurements is associated with the so-called negative IP effect (for further details, see Sumner, 1976, pp. 195–196) and is not strictly erroneous measurements. Such negative IP effects (Sumner, 1976) can be observed in two main situations: (1) adjacent to a conductor (i.e., metal) close to the electrodes, where an electrical field is enhanced within the conductor with a reversed direction to the injected current; thus, resulting in a change in the sign for measurements collected with dipoles located on different sides of the conductor and (2) layered media in which the lowest unit is more conductive than the layer immediately above and the material closest to the electrodes is polarizable.

It is also possible to observe in Figure 4 that the negative IP effects reveal good consistency between direct and reciprocal readings, supporting the argument that the negative IP effects are not erroneous measurements. In this regard, a recent study by Dahlin and Loke (2015) investigates the inversion of negative chargeability in time-domain IP, further demonstrating that those are not necessarily erroneous measurements. Hence, the negative IP effect observed in Figure 4 might be controlled by two different, and likely concurrent, conditions: (1) the water pipe located near the surface, close to electrode 40 (approximately 100 m along the profile direction) and (2) the contact between subsurface materials characterized by contrasting electrical properties at the other two anomalies (i.e., between 60 and 90 m, as well as between 120 and 180 m along the profile direction).

Additional to the detection of negative IP polarization effects, Figure 4 shows that phase-shift measurements away of the anthropogenic structures (measurements with electrodes 1–30 and electrodes 45–80) are related to lower polarization effects ($-\phi_a < 10$ mrad), with the lowest values associated with those measurements within the contaminated area ($-\phi_a < 5$ mrad). Additionally, measurements associated with larger separations between current and potential dipoles (more than 25 electrodes) reveal spatially incoherent patterns, as expected due to a decrease in the signal-to-noise ratio (S/N) for “deeper” measurements. These erratic measurements are due to

random error and low S/N leading to large discrepancies between direct and reciprocal measurements; the corresponding data points need to be removed before the inversion.

As observed in the plots presented in Figure 4, the ϕ_a values recorded close to the anthropogenic structures (the unpaved road and the water pipe) dominate over the weaker response associated to subsurface materials. Visual comparison of the plots in Figure 4 also reveals that the ϕ_a values for measurements collected between electrodes 32 and 48 vary dramatically at different times. These temporal variations in the data collected between electrodes 32 and 48 can only be explained by (1) changes in the contact resistance of the electrodes placed on the paved road and associated changes in the signal strength and (2) changes in the moisture at the contact between the soil and the water pipe due to seasonal fluctuations in the groundwater level.

The high ϕ_a values of measurements over anthropogenic structures (between electrodes 32 and 48) are not increasing the misfits between direct and reciprocal readings because those are not outliers in the independent data sets. Thus, the data error ε estimated for independent data sets cannot be used to quantify temporal distortions in the data due to cultural noise. Other methods proposed for the identification of outliers, and quantification of data quality, such as stacking (i.e., repeatability), or the analysis of the voltage-decay curve for time-domain IP readings (e.g., Gazoty et al., 2013; Flores Orozco et al., 2018), will also face the same problem, considering that the measurements over anthropogenic structures are spatially well-resolved and associated to a high S/N.

Hence, as a second step, we investigated the reciprocity of time-lapse differences to identify possible systematic errors affecting temporal variations in the measurements. Here, we refer to the difference between the measurements collected at time j ($j > 0$) and baseline measurements ($j = 0$, corresponding to data collected in May) for apparent resistivity $\Delta\rho_a$ and phase shift $\Delta\phi_a$ as

$$\Delta\rho_a = \log \rho_{aj} - \log \rho_{a0}, \quad (1)$$

$$\Delta\phi_a = \phi_{aj} - \phi_{a0}. \quad (2)$$

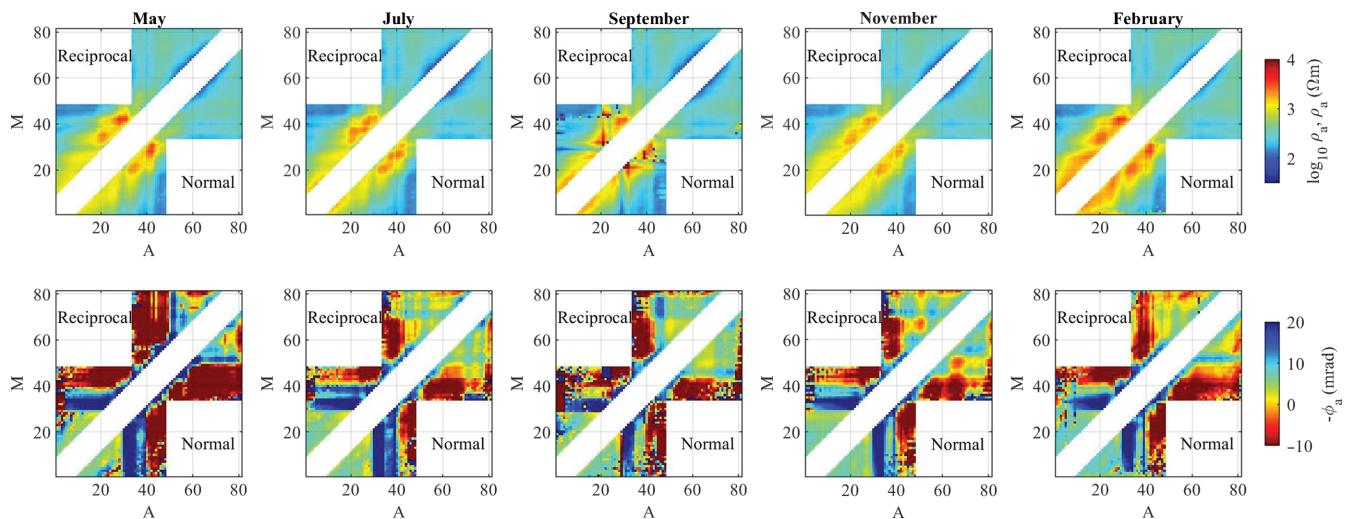


Figure 4. Plots of the raw data expressed in terms of the apparent resistivity, ρ_a (top) and impedance phase-shift ϕ_a (bottom) for each quadrupole along line A-A'. Each measurement is represented as a pixel value with the x- and y-coordinates given by the electrode number of the positive current (A) and potential (M) electrode.

We quantify the data error, at the time-lapse j , as the misfit between direct and reciprocal values of the computed time-lapse differences, which can be written for the apparent resistivity $\epsilon(\Delta\rho_a)$ as

$$\epsilon(\Delta\rho_{aj}) = \Delta\rho_{aj,D} - \Delta\rho_{aj,R}, \quad (3)$$

where $\Delta\rho_{aj,D}$ and $\Delta\rho_{aj,R}$ refer to the time-lapse difference in direct and reciprocal readings, respectively. In analogous way, the data error for time-lapse differences in phase-shift readings can be written as

$$\epsilon(\Delta\phi_{aj}) = \Delta\phi_{aj,D} - \Delta\phi_{aj,R}. \quad (4)$$

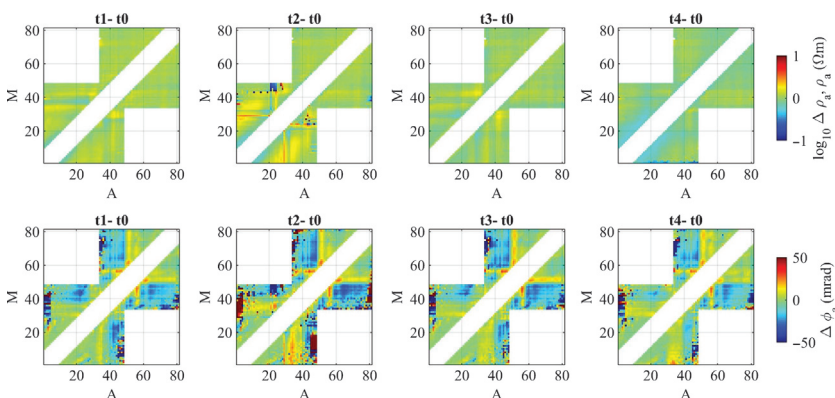


Figure 5. Plots of the time-lapse difference between baseline ($j = 0$) and time lapse ($j = 1, 2, 3, 4$) expressed in terms of the apparent resistivity, $\Delta\rho_a$ (top) and impedance phase shift $\Delta\phi_a$ (bottom) measurements in line A-A'. Each measurement is represented as a pixel value with the x - and y -coordinates given by the electrode number of the positive current (A) and potential (M) electrode.

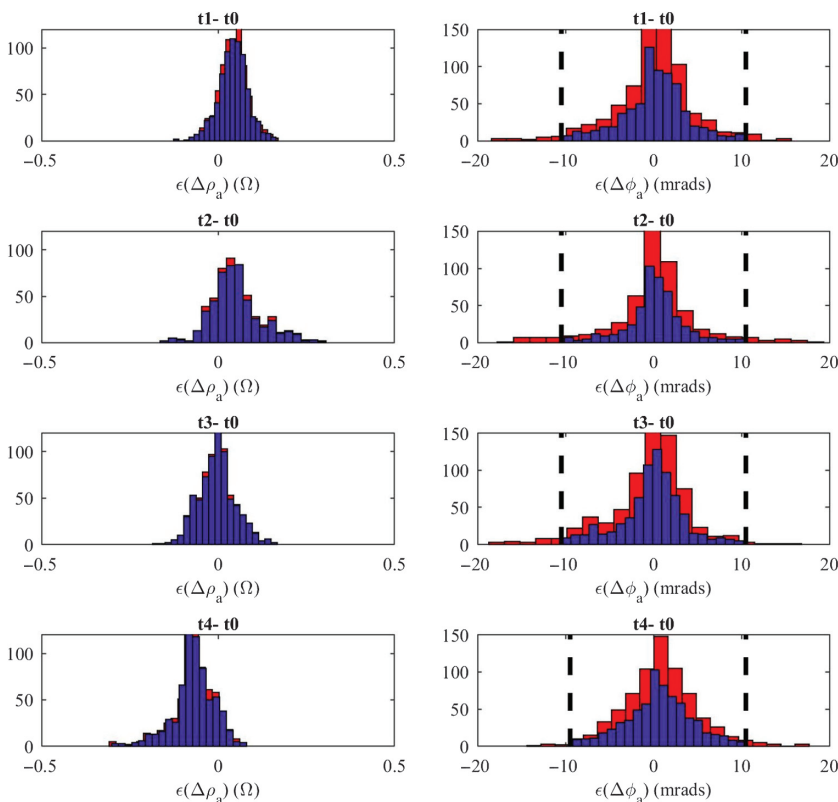


Figure 6. Plots of the data error for time-lapse differences as computed for the measured transfer resistance ($\epsilon(\Delta R)$, left) and phase-shift ($\epsilon(\Delta\phi_a)$, right). Histograms in red represent the complete time-lapse difference data set, and the imposed histogram in blue represents the resulting values after filtering the temporal outliers. The dashed lines indicate the maximum data error accepted for each time-lapse based after the analysis of misfit between direct-reciprocal time-lapse differences.

Figure 5 shows the computed time-lapse differences for data collected along line A-A'. The plots in Figure 5 reveal consistent values for the direct and reciprocal differences with the larger uncertainties observed for $\Delta\phi_a$, in measurements between electrodes 32 and 55, in the vicinity of the unpaved road, water pipe, and possible lithologic contacts. In particular, Figure 5 shows a poor reciprocity in time-lapse differences computed for readings between electrodes 50 and 55, which correspond to those electrodes installed directly on the unpaved road. Thus, such measurements could be removed before the inversion as temporal outliers.

To summarize, the outliers were identified (and removed) based on the analysis of direct-reciprocal misfit in two steps: (1) for independent data sets and (2) after the computation of the time-lapse differences ($\Delta\rho_{aj}$ and $\Delta\phi_{aj}$). In both cases, measurements were removed when the direct-reciprocal misfit exceeded the value of the corresponding average value between readings (i.e., $[\phi_{a,N} - \phi_{a,N}] > \frac{1}{2}[\phi_{a,N} + \phi_{a,R}]$). This filter assumes that measurements affected only by random error should provide a consistent value for direct and reciprocal readings for independent and time-lapse differences. From the initial 608 measurements, only 233 measuring points were used for the inversion of each independent data set, with the rest of the readings being deleted as outliers. Figures 4 and 5 demonstrate the validity of such an assumption. Histograms of the data error (i.e., $\epsilon(\Delta\rho_{aj})$ and $\epsilon(\Delta\phi_{aj})$) presented in Figure 6 demonstrate a normal distribution, as expected for random (time-lapse) data error. In addition to this, such plots reveal a few measurements related to larger $\epsilon(\Delta\phi_{aj})$ as isolated clusters separated from the main distribution of valid measurements. Hence, the occurrence of gaps in the histograms can be used to identify maximum and minimum threshold values for $\Delta\phi_{aj}$ (the dashed lines in Figure 6).

Monitoring results after removal of spatiotemporal outliers

Here, we discuss monitoring imaging results obtained from the inversion of independent data sets after the removal of temporal outliers based on the analysis of the direct-reciprocal misfit for independent measurements and time-lapse differences as described above. Furthermore, before the inversion, we removed those quadrupoles not present in all five monitoring data sets to ensure we are comparing imaging results with similar resolution

(i.e., based on the same number and distribution of quadrupoles). Accordingly, for the quantification of the data error, we performed a bin analysis as described in Flores Orozco et al. (2012b) based on the joined direct-reciprocal time-lapse misfits from all five data sets.

Hence, the error parameters were the same for the inversion of the entire monitoring data sets, following the recommendation by Lesparre et al. (2017). The underlying assumption is that by using the same error parameters, we fit all measurements to the same error level for a fair comparison of the inversion results. Such approach seems to be adequate considering that all our measurements revealed a consistent distribution of the data error (Figure 5) and of the measured ϕ_a and ρ_a values (Figures 4 and 6).

The inversion results computed for the monitoring data sets collected in line A-A' after the removal of temporal outliers following the methodology described above are presented in Figure 7. The electrical images reveal clear changes in the electrical properties for the contaminated and the clean sediments in line A-A', but most importantly, they do not reflect spatial variations between 60 and 120 m, where the anthropogenic structures (the unpaved road and the water pipe) are located. Yet, the removal of measurements close to these structures leads to a decrease of sensitivity in the computed images, as observed in the blanked pixels between 60 and 120 m. The first 60 m of profile A-A' reveal a shallow anomaly characterized by low conductivity values ($\sigma' < 1$ mS/m), the depth of which changes over time in agreement with fluctuations in the depth of the groundwater level. The high σ'

values (approximately 5 mS/m) observed in the uncontaminated area of line A-A' clearly delineate the saturated zone because they are consistently found below the groundwater table. As expected, a similar pattern is observed in the polarization (imaginary conductivity σ'') images, with low σ'' values associated with the unsaturated materials and higher values with the areas below the groundwater level. The low polarization values in the unsaturated zone show less spatial consistency, likely related to variations in the content of clay, which is polarizable even at low saturations (e.g., Titov et al., 2004). The higher σ'' values observed between May and September in the uncontaminated area at larger depths (approximately 12 m bgs) are likely to reflect the vertical contact between sand and gravel (Cassiani et al., 2004, 2014). Such contact is not visible in data sets collected for deeper positions of the groundwater table (November, February), which is explained by a decrease in the depth of investigation due to the long pathways of current injections through the unsaturated zone (Flores Orozco et al., 2013).

Regarding the contaminated area in profile A-A', here only minimal changes are observed for measurements collected at different periods. The shallow conductive unit (down to 4 m bgs) is related to the paleochannel discussed above. The interpreted high clay content in that area explains the high CC values (σ' and σ''). The response of such a layer is constant over time, thus it is not affected by the analysis of time-lapse reciprocity. Below this unit only low values for the polarization effect ($\sigma'' \ll 1$ $\mu\text{S/m}$) are observed in all monitoring images for line A-A', corresponding with the area where

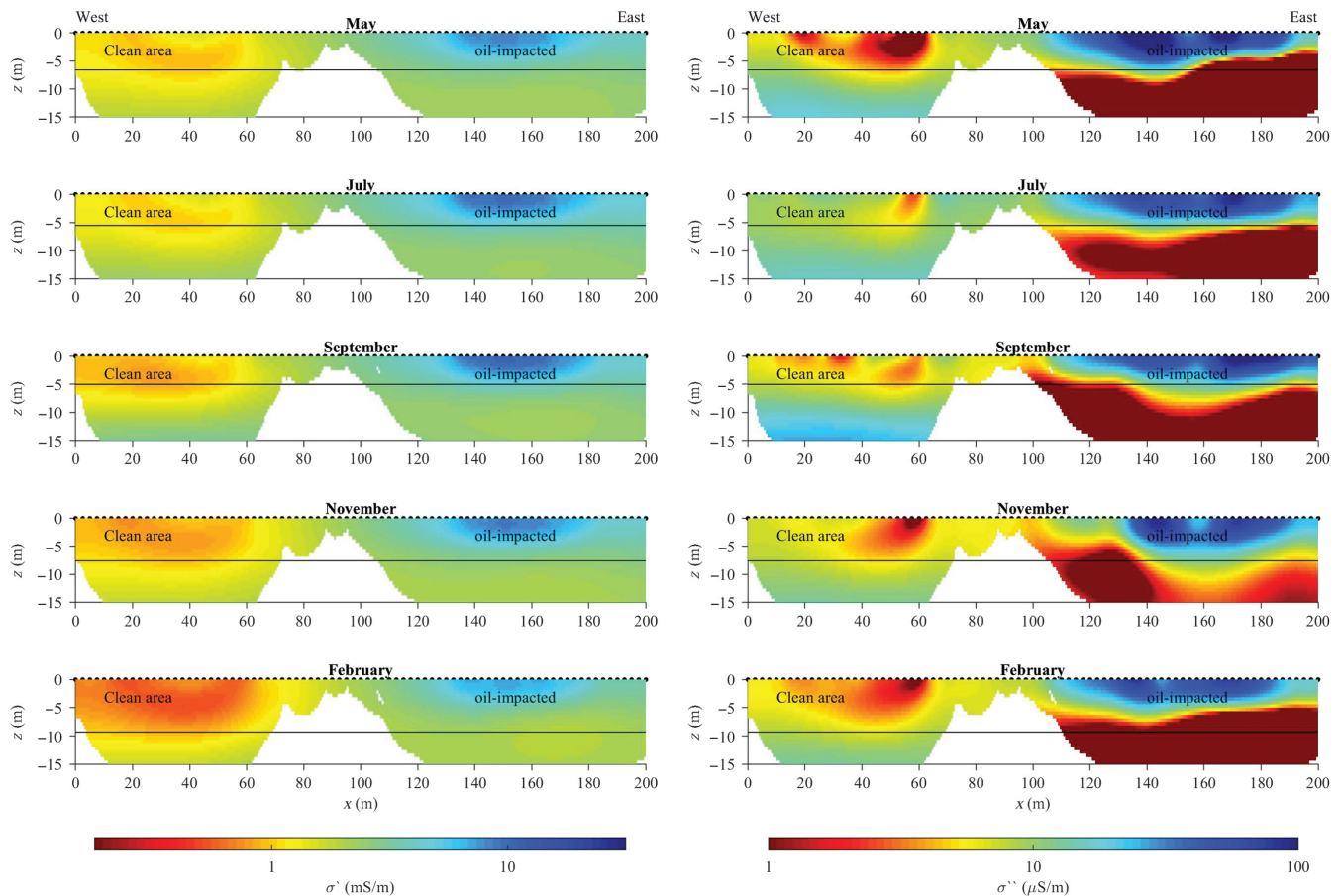


Figure 7. Monitoring imaging results after the removal of spatiotemporal outliers for data collected in line A-A' in terms of the real (left) and imaginary (right) component of the CC. The water table at each time is indicated by the solid line.

higher concentrations of hydrocarbon have been reported (and confirmed by the detailed data shown, e.g., in Cassiani et al., 2014). The geometry of the low polarization unit shows no correlation with fluctuations in the water table.

The negligible polarization effect associated with high hydrocarbon concentrations observed in Figure 7 is consistent with observations reported in the previous laboratory (Ustra et al., 2012; Personna et al., 2013) and field studies (Flores Orozco et al., 2012a; Johansson et al., 2015). However, the model proposed by Schmutz et al. (2010) does not explain the observed decrease in the polarization response, even if crude oil is mainly composed of nonpolar compounds. In this regard, some authors have argued that carbonic acids and other metabolic products might change the surface properties of hydrocarbons, promoting oil-wetting conditions (Cassidy et al., 2001; Zhao and Ioannidis, 2007). Hence, the negligible polarization response is consistent with the predicted response by the model of Revil et al. (2011).

A recent mechanistic model describing the membrane polarization for immiscible fluids trapped within the pore-space predicts a decrease in the polarization response for high concentrations of nonwetting hydrocarbons (Bücker et al., 2017). Based on the formulation of the membrane polarization, this model demonstrates that σ'' values are only dependent on the variations in the pore-space geometry imposed by the hydrocarbon droplets. Hence, the negligible polarization response observed in the contaminated area can be explained by the presence of immobile oil trapped within the micropores forming a continuous oil film with the mobile fraction occupying the macropores. As demonstrated by Bücker et al. (2017), such a continuous film hinders the formation of ion-selective membrane required for the

development of membrane polarization, and it could result in the negligible σ'' response observed in profile A-A' for the periods with a shallow water table. Accordingly, the polarization effect is still negligible for measurements between November and May, for deeper positions of the groundwater table because the oil trapped within the micropores forms a continuous film with air, another electrical insulator. Such an explanation is supported by the high TPH concentrations reported at the position of profile A-A' (Figure 1). The hindered polarization response over the entire depth, and not only on top of the saturated zone, as expected for a LNAPL such as oil, could be explained by the seasonal fluctuations in the water table depth, which transported the hydrocarbons into deeper sediments as observed in the TPH concentrations presented in Figure 1. Monitoring images in Figure 7 suggest that the sediments are not washed off following the recovery of the groundwater, which is also consistent with the persistence of the contaminant concentrations observed at the site (Cassiani et al., 2014). To support our interpretation, we present in Figure 8 the electrical properties (in terms of the σ' and σ'' values) as extracted from the electrical images from A-A' for pixel values located in the clean (30–40 m along the profile direction) and contaminated (160–170 m along the profile direction) regions at different periods, as well as the water content profile as obtained from GPR ZOP measurements performed between two boreholes located in the contaminated region practically along line A-A' (close to 150 m along profile direction) (Cassiani et al., 2014). ZOP measurements were performed at different periods associated with different depths of the groundwater level. The results indicate only relatively small changes in the water content, in agreement with the interpretation of the CC monitoring results. This is in contrast with the large moisture-content variations observed by the ZOP data at another pair of boreholes in the uncontaminated zone close to the control line B-B' (Cassiani et al., 2014). Figure 8 also reveals vertical changes between 4 and 12 m depths in the ZOP data, consistent with the limits of the clay-rich layer (4 m bgs) and with the depth interface (12 m bgs) observed in the σ'' images.

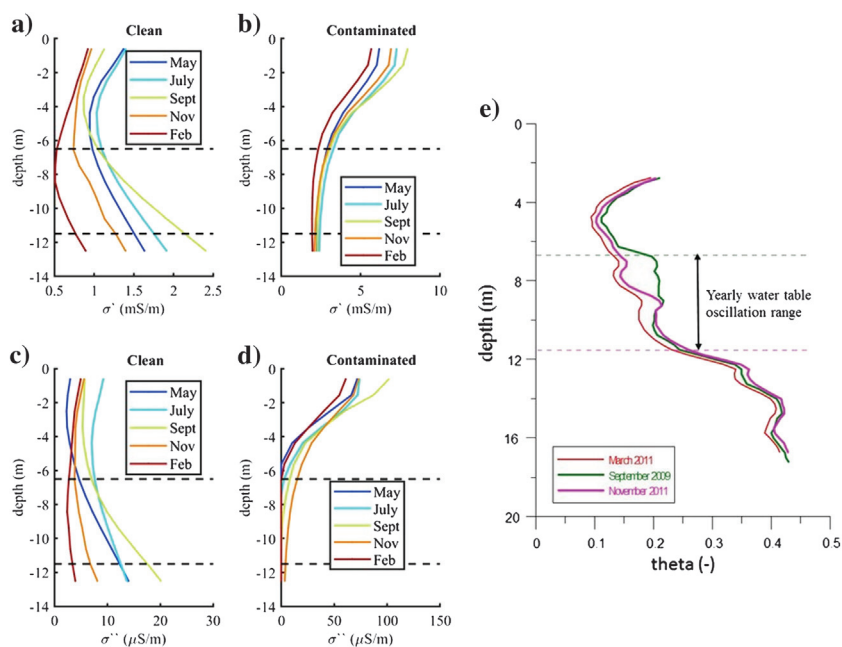


Figure 8. Temporal variations in electrical properties expressed in terms of the (a, b) real and (c, d) imaginary components of the CC for pixel values extracted from the electrical images computed for line A-A' in (a, c) clean (between 30 and 40 m along the profile direction) and (b, d) contaminated (between 160 and 170 m along the profile direction) regions. The dashed lines represent the yearly water table variations during the collection of the data (2009–2010). For comparison, (e) shows the estimated soil moisture content derived from crosshole GPR ZOP for data collected at different time instants in the heavily contaminated zone, after Cassiani et al. (2014).

the hydrocarbons act as electrical insulators; thus, the relatively high σ' observed in the contaminated sediments of profile A-A' confirms the changes in the electrical properties in mature hydrocarbon plumes due to microbial activity, e.g., the release of carbonic acids (Sauck, 2000; Werkema et al., 2003; Atekwana and Atekwana, 2010; Caterina et al., 2017). Microbial activity has been reported at the site (Burbery et al., 2004), and high concentrations of total organic carbon observed at the site (Cassiani et al., 2014) support the interpretation of the high σ' values in hydrocarbon-impacted sediments. Recent laboratory studies report an increase in the polarization effect due to the accumulation of metallic minerals accompanying the stimulation of microbial activity in soil samples obtained from hydrocarbon-contaminated sites (e.g., Mewafy et al., 2013; Atekwana and Abdel Aal, 2015). However, our results do not reveal any increase in the σ'' ; neither has the formation of iron sulfides been reported at the site.

CONCLUSION

We have presented a detailed analysis of the data error in time-lapse differences of apparent resistivity $\varepsilon(\Delta\rho_a)$ and phase-shift $\varepsilon(\Delta\phi_a)$ for monitoring CCI data sets. The data error was computed by means of the widely accepted analysis of direct and reciprocal misfit, taking it one step further to investigate the reciprocity for time-lapse differences. The CC data sets were collected in the vicinity of different anthropogenic structures, such as a water pipe, unpaved roads, and in prevalence of negative IP effects. Analysis of the independent data sets reveals that such measurements are associated with a high S/N, which also show a high correlation between direct and reciprocal measurements (variations <10% of the mean value), demonstrating that readings exhibiting a negative IP effect are not necessarily erratic measurements.

CCI results obtained after the removal of outliers in time-lapse differences revealed significant differences between the electrical signatures from clean subsurface materials and those impacted by the oil spill. For an uncontaminated region, CC images exhibited changes in agreement with seasonal variations in the position of the groundwater level; whereas contaminated sediments exhibited a constant response over the entire monitoring period associated with a negligible polarization effect and relatively high electrical conductivities. The increase in the electrical conductivity in contaminated sediments is explained by degradation processes of the contaminant plume, such as the release of carbonic acids accompanying microbial activity in mature hydrocarbon plumes. The reduction of the polarization response can be explained by the presence of hydrocarbon droplets trapped within the macro and micropores, which results in the formation of a water film surrounding grain minerals

with a constant thickness, hindering the development of ion-selective membranes and the membrane polarization.

The CCI results are consistent with independent results obtained with other geophysical methods, namely, GPR and low-induction-number EMI methods. The electrical images computed after the removal of the temporal outliers reveal no anomalies associated with anthropogenic structures validating the suitability of the proposed approach.

ACKNOWLEDGMENTS

This research was made possible by funding from the EU FP7 collaborative project ModelPROBE "Model Driven Soil Probing, Site Assessment and Evaluation." The authors thank K. Haaken, C. Oberdörster, R. Deiana, J. Boaga, M. Rossi, and A. Godio for their help in the collection of geophysical data. We appreciate L. Slater, D. Ntargiannis, and M. Weigand for the observations and comments that permitted us to improve significantly the quality of the manuscript.

DATA AND MATERIALS AVAILABILITY

Data associated with this research are available and can be obtained by contacting the corresponding author.

APPENDIX A

COMPLEX CONDUCTIVITY MONITORING PRIOR THE REMOVAL OF TEMPORAL OUTLIERS

In Figure A-1, we present the CC imaging results obtained for monitoring data collected along profile A-A' before the temporal

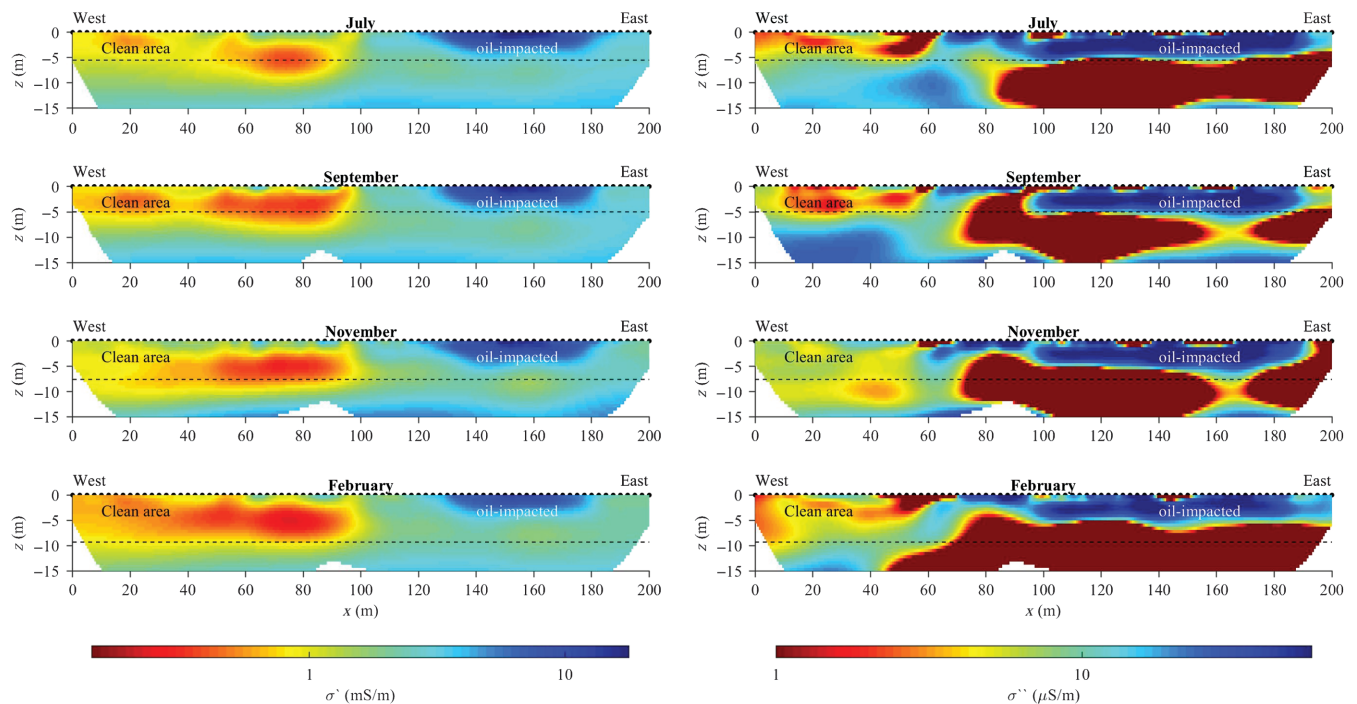


Figure A-1. The CCI results obtained for monitoring data collected at the Trecate site. Each data set was processed independently following the analysis of the misfit between direct and reciprocal readings described in Flores Orozco et al. (2012a). Accordingly, outliers and error parameters were defined independently for each data set. Imaging results are presented in terms of the real and imaginary component of the CC. The dashed line represents the position of the groundwater level at each monitoring period. The position of the electrodes is indicated at the surface by the black points.

analysis of reciprocity in time-lapse differences and the removal of temporal outliers. Images presented in Figure A-1 show a poor consistency with temporal variations of the groundwater level, for both contaminated and uncontaminated areas. Plots in Figure A-1 clearly reveal the limitations of reciprocal analysis in monitoring data sets, in particular for measurements collected in areas affected by cultural noise.

REFERENCES

- Abdel Aal, G. Z., E. A. Atekwana, and A. Revil, 2014, Geophysical signatures of disseminated iron minerals: A proxy for understanding subsurface biophysicochemical processes: *Journal of Geophysical Research: Biogeosciences*, **119**, 1831–1849.
- Abdel Aal, G. Z., L. D. Slater, and E. A. Atekwana, 2006, Induced-polarization measurements on unconsolidated sediments from a site of active hydrocarbon biodegradation: *Geophysics*, **71**, no. 2, H13–H24, doi: [10.1190/1.2187760](https://doi.org/10.1190/1.2187760).
- Archie, G. E., 1942, The electrical resistivity log as an aid in determining some reservoir characterization: *Transactions of the American Institute of Mining, Metallurgical, and Petroleum Engineers*, **146**, 54–62.
- Atekwana, E. A., and G. Z. Abdel Aal, 2015, Iron biomineralization controls on geophysical signatures of hydrocarbon contaminated sediments: *Journal of Earth Science*, **26**, 835–843, doi: [10.1007/s12583-015-0611-2](https://doi.org/10.1007/s12583-015-0611-2).
- Atekwana, E. A., and E. A. Atekwana, 2010, Geophysical signatures of microbial activity at hydrocarbon contaminated sites: A review: *Survey of Geophysics*, **31**, 247–283, doi: [10.1007/s10712-009-9089-8](https://doi.org/10.1007/s10712-009-9089-8).
- Atekwana, E. A., E. A. Atekwana, D. D. Werkema, P. J. Allen, L. A. Smart, J. W. Duris, D. P. Cassidy, W. A. Sauck, and S. Rossbach, 2004, Evidence for microbial enhanced electrical conductivity in hydrocarbon-contaminated sediments: *Geophysical Research Letters*, **31**, L23501.
- Atekwana, E. A., and L. D. Slater, 2009, Biogeophysics: A new frontier in earth science research: *Reviews of Geophysics*, **47**, RG4004, doi: [10.1029/2009RG000285](https://doi.org/10.1029/2009RG000285).
- Binley, A., J. Keery, L. Slater, W. Barrash, and M. Cardiff, 2016, The hydrogeologic information in cross-borehole complex conductivity data from an unconsolidated conglomeratic sedimentary aquifer: *Geophysics*, **81**, no. 6, E409–E421, doi: [10.1190/geo2015-0608.1](https://doi.org/10.1190/geo2015-0608.1).
- Brandt, C. A., J. M. Becker, and A. Porta, 2002, Distribution of polycyclic aromatic hydrocarbons in soils and terrestrial biota after a spill of crude oil in Trecate, Italy: *Environmental Toxicology Chemistry*, **21**, 1638–1643, doi: [10.1002/etc.v21.8](https://doi.org/10.1002/etc.v21.8).
- Bücker, M., A. Flores Orozco, A. Hördt, and A. Kemna, 2017, An analytical membrane-polarization model to predict the complex conductivity signature of immiscible liquid hydrocarbon contaminants: *Near Surface Geophysics*, **15**, 547–562.
- Burbery, L., G. Cassiani, G. Andreotti, T. Ricchiuto, and K. T. Semple, 2004, Well test and stable isotope analysis for the determination of sulphate-reducing activity in a fast aquifer contaminated by hydrocarbons: *Environmental Pollution*, **129**, 321–330, doi: [10.1016/j.envpol.2003.10.017](https://doi.org/10.1016/j.envpol.2003.10.017).
- Cassiani, G., A. Binley, A. Kemna, M. Wehrer, A. Flores Orozco, R. Deiana, J. Boaga, M. Rossi, P. Dietrich, U. Werban, L. Zschornack, A. Godio, A. JafarGandomi, and G. P. Deidda, 2014, Non-invasive characterization of the Trecate (Italy) crude-oil contaminated site: Links between contamination and geophysical signals: *Environmental Science and Pollution Research*, Special Issue on New approaches for low-invasive contaminated site characterization, monitoring and modeling, **21**, 8914–8931, doi: [10.1007/s11356-014-2494-7](https://doi.org/10.1007/s11356-014-2494-7).
- Cassiani, G., A. Kemna, A. Villa, and E. Zimmermann, 2009, Spectral induced polarization for the characterization of free-phase hydrocarbon contamination of sediments with low clay content: *Near Surface Geophysics*, **7**, 547–562.
- Cassiani, G., C. Strobbia, and L. Gallotti, 2004, Vertical radar profiles for the characterization of deep vadose zones: *Vadose Zone Journal*, **3**, 1093–1115, doi: [10.2136/vzj2004.1093](https://doi.org/10.2136/vzj2004.1093).
- Cassidy, D. P., D. D. Werkema, Jr., W. Sauck, E. Atekwana, S. Rossbach, and J. Duris, 2001, The effects of LNAPL biodegradation products on electrical conductivity measurements: *Journal of Environmental and Engineering Geophysics*, **6**, 47–52, doi: [10.4133/JEEG6.1.47](https://doi.org/10.4133/JEEG6.1.47).
- Caterina, D., A. Flores Orozco, and F. Nguyen, 2017, Long-term ERT monitoring of biogeochemical changes of an aged hydrocarbon contamination: *Journal of Contaminant Hydrology*, **201**, 19–29, doi: [10.1016/j.jconhyd.2017.04.003](https://doi.org/10.1016/j.jconhyd.2017.04.003).
- Chambers, J. E., P. I. Meldrum, R. D. Ogilvy, and P. B. Wilkinson, 2005, Characterization of a NAPL-contaminated former quarry site using electrical impedance tomography: *Near Surface Geophysics*, **3**, 79–90, doi: [10.3997/1873-0604.2005003](https://doi.org/10.3997/1873-0604.2005003).
- Dahlin, T., and M. H. Loke, 2015, Negative apparent chargeability in time-domain induced polarization data: *Journal of Applied Geophysics*, **123**, 322–332, doi: [10.1016/j.jappgeo.2015.08.012](https://doi.org/10.1016/j.jappgeo.2015.08.012).
- Deceuster, J., and O. Kaufmann, 2012, Improving the delineation of hydrocarbon impacted soils and water through induced polarization (IP) tomographies: A field study at an industrial waste land: *Journal of Contaminant Hydrology*, **136**, 25–42, doi: [10.1016/j.jconhyd.2012.05.003](https://doi.org/10.1016/j.jconhyd.2012.05.003).
- Flores Orozco, A., J. Gallistl, M. Bücker, and K. H. Williams, 2018, Decay curve analysis for data error quantification in time-domain induced polarization imaging: *Geophysics*, **83**, no. 2, E75–E86, doi: [10.1190/geo2016-0714.1](https://doi.org/10.1190/geo2016-0714.1).
- Flores Orozco, A., A. Kemna, C. Oberdörster, L. Zschornack, C. Leven, P. Dietrich, and H. Weiss, 2012a, Delineation of subsurface hydrocarbon contamination at a former hydrogenation plant using spectral induced polarization imaging: *Journal of Contaminant Hydrology*, **136**–137, 131–144, doi: [10.1016/j.jconhyd.2012.06.001](https://doi.org/10.1016/j.jconhyd.2012.06.001).
- Flores Orozco, A., A. Kemna, and E. Zimmermann, 2012b, Data error quantification in spectral induced polarization imaging: *Geophysics*, **77**, no. 3, E227–E237, doi: [10.1190/geo2010-0194.1](https://doi.org/10.1190/geo2010-0194.1).
- Flores Orozco, A., M. Velimirovic, T. Tosco, A. Kemna, H. Sapion, N. Klaas, R. Sethi, and B. Leen, 2015, Monitoring the injection of microscale zero-valent iron particles for groundwater remediation by means of complex electrical conductivity imaging: *Environmental Science and Technology*, **49**, 5593–5600, doi: [10.1021/acs.est.5b00208](https://doi.org/10.1021/acs.est.5b00208).
- Flores Orozco, A., H. K. Williams, and A. Kemna, 2013, Time-lapse spectral induced polarization imaging of stimulated uranium bioremediation: *Near Surface Geophysics*, **11**, 531–544, doi: [10.3997/1873-0604.2013020](https://doi.org/10.3997/1873-0604.2013020).
- Flores Orozco, A., H. K. Williams, P. E. Long, S. S. Hubbard, and A. Kemna, 2011, Using complex resistivity imaging to infer biogeochemical processes associated with bioremediation of an uranium-contaminated aquifer: *Journal of Geophysical Research*, **116**, G03001, doi: [10.1029/2010JG001591](https://doi.org/10.1029/2010JG001591).
- Gazoty, A., G. Fiandaca, J. Pedersen, E. Auken, and A. V. Christiansen, 2013, Data repeatability and acquisition techniques for time-domain spectral induced polarization: *Near Surface Geophysics*, **11**, 391–406.
- Heenan, J., L. D. Slater, D. Ntarlagiannis, E. A. Atekwana, B. Z. Fathepure, S. Dalvi, C. Ross, D. D. Werkema, and E. A. Atekwana, 2014, Electrical resistivity imaging for long-term autonomous monitoring of hydrocarbon degradation: Lessons from the deepwater Horizon oil spill: *Geophysics*, **80**, no. 1, B1–B11, doi: [10.1190/geo2013-0468.1](https://doi.org/10.1190/geo2013-0468.1).
- Johansson, S., G. Fiandaca, and T. Dahlin, 2015, Influence of non-aqueous phase liquid configuration on induced polarization parameters: Conceptual models applied to a time-domain field case study: *Journal of Applied Geophysics*, **123**, 295–309, doi: [10.1016/j.jappgeo.2015.08.010](https://doi.org/10.1016/j.jappgeo.2015.08.010).
- Kemna, A., 2000, Tomographic inversion of complex resistivity: Theory and application: Ph.D. thesis, Ruhr-University of Bochum.
- Kemna, A., A. Binley, G. Cassiani, E. Niederleithinger, A. Revil, L. Slater, K. H. Williams, A. Flores Orozco, F. H. Haegel, A. Hördt, S. Kruschwitz, V. Leroux, K. Titov, and E. Zimmermann, 2012, An overview of the spectral induced polarization method for near-surface applications: *Near Surface Geophysics*, **10**, 453–468.
- Kemna, A., A. Binley, and L. Slater, 2004, Crosshole IP imaging for engineering and environmental applications: *Geophysics*, **69**, 97–107, doi: [10.1190/1.1649379](https://doi.org/10.1190/1.1649379).
- Kemna, A., E. Räkera, and A. Binley, 1997, Application of complex resistivity tomography to field data from a Kerosene-contaminated site: *Proceedings of the 3rd Meeting Environmental and Engineering Geophysics*, European Section, 151–154.
- Kemna, A., J. Vanderborght, B. Kulesha, and H. Vereecken, 2002, Imaging and characterization of subsurface solute transport using electrical resistivity tomography (ERT) and equivalent transport models: *Journal of Hydrology*, **267**, 125–146, doi: [10.1016/S0022-1694\(02\)00145-2](https://doi.org/10.1016/S0022-1694(02)00145-2).
- Lesparre, N., F. Nguyen, A. Kemna, T. Robert, T. Hermans, M. Daoudi, and A. Flores Orozco, 2017, A new approach for time-lapse data weighting in electrical resistivity tomography: *Geophysics*, **82**, no. 6, E325–E333, doi: [10.1190/geo2017-0024.1](https://doi.org/10.1190/geo2017-0024.1).
- Marshall, D., and T. Madden, 1959, Induced polarization, a study of its causes: *Geophysics*, **24**, 790–816, doi: [10.1190/1.1438659](https://doi.org/10.1190/1.1438659).
- Mewafy, F. M., D. D. Werkema, E. A. Atekwana, L. D. Slater, G. Z. Abdel Aal, A. Revil, and D. Ntarlagiannis, 2013, Evidence that bio-metallic mineral precipitation enhances the complex conductivity response at a hydrocarbon contaminated site: *Journal of Applied Geophysics*, **98**, 113–123, doi: [10.1016/j.jappgeo.2013.08.011](https://doi.org/10.1016/j.jappgeo.2013.08.011).
- Naudet, V., J. C. Gourry, F. Girard, F. Mathieu, and A. Saada, 2014, 3D electrical resistivity tomography to locate DNAPL contamination around a housing estate: *Near Surface Geophysics*, **12**, 351–360, doi: [10.3997/1873-0604.2012059](https://doi.org/10.3997/1873-0604.2012059).
- Olhoeft, G. R., 1985, Low-frequency electrical-properties: *Geophysics*, **50**, 2492–2503, doi: [10.1190/1.1441880](https://doi.org/10.1190/1.1441880).

- Personna, Y. R., L. Slater, D. Ntarlagiannis, D. Werkema, and Z. Szabo, 2013, Complex resistivity signatures of ethanol biodegradation in porous media: *Journal of Contaminant Hydrology*, **153**, 37–50, doi: [10.1016/j.jconhyd.2013.07.005](https://doi.org/10.1016/j.jconhyd.2013.07.005).
- Revil, A., E. Atekwana, C. Zhang, A. Jardani, and S. Smith, 2012, A new model for the spectral induced polarization signature of bacterial growth in porous media: *Water Resources Research*, **48**, W09545.
- Revil, A., M. Schmutz, and M. L. Batzle, 2011, Influence of oil wettability upon spectral induced polarization of oil-bearing sands: *Geophysics*, **76**, no. 5, A31–A36, doi: [10.1190/geo2011-0006.1](https://doi.org/10.1190/geo2011-0006.1).
- Sauck, W. A., 2000, A model for the resistivity structure of LNAPL plumes and their environs in sandy sediments: *Journal of Applied Geophysics*, **44**, 151–165, doi: [10.1016/S0926-9851\(99\)00021-X](https://doi.org/10.1016/S0926-9851(99)00021-X).
- Schädler, S., M. Morio, S. Bartke, and M. Finkel, 2012, Integrated planning and spatial evaluation of megasite remediation and reuse options: *Journal of Contaminant Hydrology*, **127**, 88–100, doi: [10.1016/j.jconhyd.2011.03.003](https://doi.org/10.1016/j.jconhyd.2011.03.003).
- Schmutz, M., A. Revil, P. Vaudelet, M. Batzle, P. F. Vĩfiao, and D. D. Werkema, 2010, Influence of oil saturation upon spectral induced polarization of oil-bearing sands: *Geophysical Journal International*, **183**, 211–224, doi: [10.1111/j.1365-246X.2010.04751.x](https://doi.org/10.1111/j.1365-246X.2010.04751.x).
- Slater, L., and D. Lesmes, 2002, Electrical-hydraulic relationships observed for unconsolidated sediments: *Water Resources Research*, **38**, 31–31-13, doi: [10.1029/2001WR001075](https://doi.org/10.1029/2001WR001075).
- Slater, L., D. Ntarlagiannis, Y. R. Personna, and S. Hubbard, 2007, Pore-scale spectral induced polarization (SIP) signatures associated with FeS biomineral transformations: *Geophysical Research Letters*, **34**, L21404, doi: [10.1029/2007GL031840](https://doi.org/10.1029/2007GL031840).
- Sumner, J. S., 1976, *Principles of induced polarization for geophysical exploration*: Elsevier Science Publishing Co.
- Titov, K., A. Kemna, A. Tarasov, and H. Vereecken, 2004, Induced polarization of unsaturated sands determined through time domain measurements: *Vadose Zone Journal*, **3**, 1160–1168, doi: [10.2136/vzj2004.1160](https://doi.org/10.2136/vzj2004.1160).
- Ustra, A., L. Slater, D. Ntarlagiannis, and V. Elis, 2012, Spectral induced polarization (SIP) signatures of clayey soils containing toluene: *Near Surface Geophysics*, **10**, 503–515, doi: [10.3997/1873-0604.2012015](https://doi.org/10.3997/1873-0604.2012015).
- Vanhala, H., 1997, Mapping oil-contaminated sand and till with the spectral induced polarization (SIP) method: *Geophysical Prospecting*, **45**, 303–326, doi: [10.1046/j.1365-2478.1997.00338.x](https://doi.org/10.1046/j.1365-2478.1997.00338.x).
- Von Hippel, A. R., 1954, *Dielectric and waves*: John Wiley and Sons.
- Weigand, M., A. Flores Orozco, and A. Kemna, 2017, Reconstruction quality of SIP parameters in multi-frequency complex resistivity imaging: *Near Surface Geophysics*, **15**, 187–199.
- Werkema, D. D., E. A. Atekwana, A. L. Endres, W. A. Sauck, and D. P. Cassidy, 2003, Investigating the geoelectrical response of hydrocarbon contamination undergoing biodegradation: *Geophysical Research Letters*, **30**, 49, doi: [10.1029/2003GL017346](https://doi.org/10.1029/2003GL017346).
- Williams, P. F., and B. R. Rust, 1969, The sedimentology of a braided river: *Journal of Sedimentary Research*, **39**, 1641–1643, doi: [10.1306/74D71EE2-2B21-11D7-8648000102C1865D](https://doi.org/10.1306/74D71EE2-2B21-11D7-8648000102C1865D).
- Zhao, W., and M. A. Ioannidis, 2007, Effect of NAPL film stability on the dissolution of residual wetting NAPL in porous media: A pore-scale modeling study: *Advances in Water Resources*, **30**, 171–181, doi: [10.1016/j.advwatres.2005.03.025](https://doi.org/10.1016/j.advwatres.2005.03.025).